arXiv:1512.00117v1 [cond-mat.stat-mech] 1 Dec 2015

Transition from compact to porous films in deposition with temperature activated diffusion

Dung di Caprio[1,a]
F. D. A. Aarão Reis[2,b]

(1) PSL Research University, Chimie ParisTech - CNRS, Institut de Recherche de Chimie Paris, 75005, Paris, France
(2) Instituto de Física, Universidade Federal Fluminense, Avenida Litorânea s/n, 24210-340 Niterói RJ, Brazil

(Dated: December 2, 2015)

We study a thin film growth model with temperature activated diffusion of adsorbed particles, allowing for the formation of overhangs and pores, but without detachment of adatoms or clusters from the deposit. Simulations in one-dimensional substrates are performed for several values of the diffusion-to-deposition ratio R of adatoms with a single bond and of the detachment probability ϵ per additional nearest neighbor (NN), respectively with activation energies are E_s and E_b. If R and ϵ independently vary, regimes of low and high porosity are separated at $0.075 \leq \epsilon_c \leq 0.09$, with vanishingly small porosity below that point and finite porosity for larger ϵ. Alternatively, for fixed values of E_s and E_b and varying temperature, the porosity has a minimum at T_c, and a nontrivial regime in which it increases with temperature is observed above that point. This is related to the large mobility of adatoms, resembling features of equilibrium surface roughening. In this high-temperature region, the deposit has the structure of a critical percolation cluster due to the non-desorption. The pores are regions enclosed by blobs of the corresponding percolating backbone, thus the distribution of pore size s is expected to scale as $s^{-\tilde{\tau}}$ with $\tilde{\tau} \approx 1.45$, in reasonable agreement with numerical estimates. Roughening of the outer interface of the deposits suggests Villain-Lai-Das Sarma scaling below the transition. Above the transition, the roughness exponent $\alpha \approx 0.35$ is consistent with the percolation backbone structure via the relation $\alpha = 2 - d_B$, where d_B is the backbone fractal dimension.

[a] Email address: dung.di-caprio@chimie-paristech.fr
[b] Email address: reis@if.uff.br

I. INTRODUCTION

Porous materials attract much interest due to their broad range of commercial and scientific applications [1–4]. Tailoring of materials with the desired structure, physical, and chemical properties has been mainly an empirical work. However, modeling the effects of growth conditions on those properties may be a useful tool to improve them. For instance, for applications of porous films of oxides or silicon, the simultaneous regulation of porosity and surface roughness is suggested in Refs. [5, 6].

In the study of thin porous film, the simplest models probably are ballistic deposition (BD) [7, 8] and its extensions [9–12]. In these models, the surface relaxation processes take place during a short time interval after the aggregation of incident particles (atoms, molecules, or clusters). Changes of growth parameters may lead to drastic changes in the porosity and pore connectivity of the deposits, typically with the porosity decreasing as surface relaxation processes are enhanced [9, 13–16].

Compact structures are usually observed in film growth dominated by surface diffusion, particularly if diffusion lengths of adsorbed species are large [8, 17]. Some models with activated diffusion of adsorbed species may produce porous deposits at low temperatures, but the porosity decreases as the substrate temperature increases [18, 19]. In experiments and models, the formation of larger crystalline grains and smoother film surfaces are also observed as the substrate temperature increases [20].

The opposite trend is observed in some systems, such as electrostatic spray deposition of oxides [21, 22]: transitions from compact to ramified structures occur as the temperature increases. Other physico-chemical parameters are also related to these features, such as the liquid content of the spray droplets. For instance, solution evaporation and clustering in those droplets before adsorption is suggested to explain the formation of ramified structures [21]. However, the results also suggest to investigate whether surface diffusion of adsorbed atoms or molecules may lead to increase of film porosity or roughness.

In this paper, we introduce a model of thin film deposition with no desorption and with temperature activated adatom diffusion that shows this trend at high temperatures. It is an extension of the Clarke-Vvedensky (CV) model for thin film growth [17, 23] without the usual solid-on-solid condition and without desorption. For fixed value of binding energies, there is a (low temperature) regime with porosity decreasing with temperature and, above a transition point, a regime with porosity increasing with temperature. In the latter regime, the deposit has a critical percolation backbone structure, which is reflected in the roughness scaling, and the pore size distribution has a power-law decay related to percolation exponents. This suggests an alternative interpretation for the increase of porosity in high temperature deposition processes and the possibility of producing critical pore size distributions in a broad range of growth parameters.

The rest of this paper is organized as follows. In Sec. II, we present the deposition model and the simulation procedure. In Sec. III, we analyze the internal structure of the deposits, focusing on the changes of porosity as the model parameters change. In Sec. IV, we present the pore size distributions obtained in simulations and explain their high-temperature decay using percolation concepts. In Sec. V, we discuss the surface roughness scaling in the deposits. In Sec. VI, we summarize our results and present our conclusions.

II. MODEL AND SIMULATION PROCEDURE

Deposition occurs in a one-dimensional substrate of linear size L, with the lattice constant taken as the length unit. Periodic boundary conditions are considered in the lateral direction (x). The surface is flat at $t = 0$, with all columns with height $z = 0$.

There is an external flux of F atoms per site per unit time. The incident atom is adsorbed

upon landing above a previously deposited atom or a substrate site. After adsorption, it executes activated diffusion steps with rules described below. There is no relaxation to lower heights of neighboring columns immediately after adsorption, in contrast to the models of Refs. [18, 19, 30].

Fig. 1 highlights the adatoms that are allowed to move in a given configuration of the deposit and shows the possible steps of five of them.

The hopping rate (diffusion coefficient) $\mathcal{D}$ of an adatom at a given position depends only on the configuration of the four nearest neighbor (NN) sites of this position: $(x+1, y)$, $(x-1, y)$, $(x, y-1)$, and $(x, y+1)$. That rate does not depend on the configuration of the target position (i. e. the position after the step). Its general form is

$$\mathcal{D} = D\epsilon^{n-1}, \tag{1}$$

where n is the number of occupied NN sites and $\epsilon < 1$ because NN bonds reduce the adatom mobility. Due to the choice of length unit, $\mathcal{D}$ is the number of random steps of the adatom per unit time. Conversely, the average time for a step of this adatom is

$$\tau = 1/\mathcal{D}. \tag{2}$$

In Fig. 1, adatoms A and D have $n = 1$ ($\mathcal{D} = D$), adatom C has $n = 2$ ($\mathcal{D} = D\epsilon$), and adatoms B and E have $n = 3$ ($\mathcal{D} = D\epsilon^2$). Note that a site of the substrate is included in the neighborhood of E.

The target position of the adatom step is randomly chosen among the NN and the next nearest neighbor (NNN) sites; the latter option includes positions $(x+1, y+1)$, $(x-1, y-1)$, $(x+1, y-1)$, and $(x-1, y+1)$. The target site may be in a height above or below the current level of the adatom. The step is executed if the target site is empty and if a constraint is satisfied: all adatoms remain connected to the substrate by a set of NN adatoms after the step. This constraint prevents adatom desorption, which is a reasonable approximation for many vapor growth processes.

In Fig. 1, the adatoms in black cannot move because any step to an empty NN or NNN site would disconnect them or disconnect other adatoms from the substrate. The other adatoms are mobile, but some steps to NN or NNN sites are not allowed due to the non-desorption condition. Fig. 1 also shows the allowed steps of five labeled adatoms. The case of adatom B is particularly interesting: if it is removed, a part of the deposit is disconnected, but if it moves down-left, connectivity is restored. For this reason, this is the only acceptable step of adatom B.

The diffusion coefficient of an adatom with a single NN is related to the temperature as

$$D = h \exp\left(-E_s/k_B T\right), \tag{3}$$

where E_s is an energy barrier and h is a characteristic frequency chosen as $h = 10^{12} s^{-1}$. The reduction factor for additional NN is

$$\epsilon = \exp\left(-E_b/k_B T\right), \tag{4}$$

where E_b is a bond energy. These rules are the same of the solid-on-solid CV model in square or simple cubic lattice [23, 24]. However, in contrast to the original CV model, here the adatom is also allowed to step to empty NNN sites and the target position may be at any height, which leads to overhang formation.

In the CV model, E_s is interpreted as an interaction energy between the adatom and the atomic layers below it, while E_b is the interaction energy with in-plane (lateral) neighbors. Our model allows the formation of surface overhangs and pores, thus many adatoms do not have atomic layers below them; this is the case of adatoms A, C, and D in Fig. 1. For this reason, here E_s is interpreted as a result of interactions of the adatom with a large surrounding region, possibly including distant

neighbors. On the other hand, E_b is still interpreted as a binding energy per additional NN. This justifies the use of different values for E_s and E_b, similarly to the CV model [23, 24].

The relative effects of diffusion and deposition are represented by the ratio

$$R \equiv \frac{D}{F} = \frac{h}{F} \exp\left(-E_s/k_B T\right). \tag{5}$$

Thus, R and ϵ are taken as the model parameters for our simulations.

Simulations of the model with large values of R (of order 10^9 or more) are usual in submonolayer growth studies [25, 26], but demand long simulation times. The process of checking the connectivity of a deposit also consumes much computational time because it requires searching for possible isolated clusters [27] after the random step of an adatom. Moreover, the time for this checking increases with film thickness.

For those reasons, our simulations were restricted to two dimensions and relatively low values of R, ranging from 10^1 to 10^4. The values of ϵ were chosen in the range from 0.01 to 0.15, which is sufficient to identify a transition in the porosity scaling. For R ranging from 10 to 10^3, the lateral size of the deposits and the number of deposited layers is 400. For the largest value $R = 10^4$, the lateral size remains the same but the number of deposited layers is 100. Due to the formation of pores, the average film height may significantly exceed the number of deposited layers, particularly for large values of ϵ and R.

The porosity P is calculated in the middle of the deposits, with heights varying from 40 to $\overline{h} - 40$, where $\overline{h}$ is the average height of the outer surface (highest particles in each substrate column). P is defined as the ratio between the number of empty lattice sites and the total number of sites in the scanned region. The choice of the boundary of this region is suitable to eliminate effects of the substrate and not to reach the outer surface (note, for instance, that the roughness of the samples is always below 10 lattice units). This procedure parallels that proposed in Ref. [28] for measuring porosity is ballistic-like deposits, which consists in selecting only points below the deepest through of the samples.

The surface roughness of the deposits was also measured. In a deposit with overhangs, the height of a given column is defined as the height of the topmost particle at that column. This set of heights defines the outer surface of the deposit. For calculating the local roughness, a square box of lateral size r glides along the film surface and, at each position, the root-mean-square (rms) height fluctuation of columns inside the box is calculated. The average rms fluctuation among all box positions and among different configurations of the deposit at time t is the local roughness $w\left(r,t\right)$. The global roughness $W\left(t\right)$ is measured in the full system size L, i. e. $W\left(t\right) = w\left(L,t\right)$.

III. STRUCTURE OF THE DEPOSITS

Fig. 2 shows deposits grown with $R = 10$ and several values of ϵ. Their porosity slowly increases with ϵ, from $P \approx 0.16$ for $\epsilon = 0.01$ to $P \approx 0.28$ for $\epsilon = 0.15$. This value of R is typical of very low temperature or very large surface energy (E_s), leading to a very low adatom mobility in the time scale of deposition of an atomic layer. Increasing ϵ does not compensate this overall low mobility.

Fig. 3 shows very different features in deposits grown with $R = 10^4$: the porosity is negligible for small ϵ (smaller than 1%), but reaches $P \approx 50\%$ for $\epsilon = 0.15$.

For low ϵ (low NN binding energy), $R = 10^4$ provides large diffusion lengths for the adatoms with a small number of NN. Thus, they tend to aggregate in positions with large numbers of NNs, in which the small ϵ value warrants a long residence time. This explains the formation of compact deposits. However, for $\epsilon \sim 0.1$ or larger, the stability of positions with many NNs disappears. All adatoms can easily move, forming overhangs and pores, with connectivity preserved by constraint on allowed steps.

The porosity of deposits for several values of R is shown in Fig. 4 as a function of ϵ. It indicates the presence of a dynamic transition in the large R limit: vanishingly small porosity for $\epsilon \leq 0.075$ and finite porosity for $\epsilon \geq 0.09$. The transition point is thus estimated as $0.075 < \epsilon_c < 0.09$.

This value of ϵ_c is large, thus the corresponding binding energy E_b is of the same order of thermal energy fluctuations. In terms of that energy, the transition temperature is estimated as

$$0.386 < k_B T_c / E_b < 0.415. \tag{6}$$

This reminds the large roughening temperatures of thermal equilibrium roughening (of the same order of melting temperatures) [8, 29].

The above discussion considers R and ϵ as independent parameters. However, for a given material, E_s and E_b are fixed and related to its physico-chemical properties. Thus, R and ϵ simultaneously change, being related as

$$R = \frac{h}{F} \epsilon^{E_s/E_b}. \tag{7}$$

This is the basis to investigate the temperature dependence of the porosity.

The data in Fig. 4 for each value of R was fitted to provide a continuous approximation of P as a function of ϵ. The fitting curves were logistic functions of the form $f(x) = a_2/\left[1 + \exp\left(-a_0 - a_1 x\right)\right]$, with constants a_0, a_1, and a_2 obtained from least squares fits. For a fixed ratio E_s/E_b and a given value of R, ϵ is calculated by Eq. (7) and those fits are used to determine P.

Fig. 5 shows P versus R for five values of E_s/E_b, with fixed $h/F = 10^{12}$. Some temperature values are also indicated. For a given ratio E_s/E_b, P changes from a decreasing to an increasing function of temperature at a transition point, which is the minimum of the correspondig curve in that plot. For the smallest values of E_s/E_b in Fig. 5, extrapolation of the results in Eqs. (6) and (7) indicates that the transition occurs only for very large R. For instance, for $E_s = E_b$, the transition value is estimated as $R_c \sim 10^{11}$; for $E_s/E_b = 5$, the transition value drops to $R_c \sim 10^6$ (if $E_s = 0.5eV$ and $E_b = 0.1eV$, it gives $T_c \sim 450K$).

For $R < R_c$ (or $T < T_c$), the decrease of porosity with the temperature is qualitatively similar to results of related models [18, 19, 30]. In Ref. [18], the activation energy $0.6eV$ and maximal temperature $700K$ give maximal values of ϵ of order 10^{-4}, which is in the low temperature regime, even in a triangular lattice structure. The same range of parameters were considered in Ref. [19]. Ref. [30] showed formation of compact branches in the high temperature growth of some samples, but this was an effect of a particular lattice structure that suppressed some atomic steps, leading to an unstable growth. Similar mechanisms are not present in our model.

The nontrivial result of this model is the porosity increase with the temperature for $R > R_c$ ($T > T_c$), which was not shown in previous works. In the transition point, ϵ is not very small, thus the hopping rates have a relatively weak dependence on the number of NN. This leads to a high disorder in the distribution of adatom position, subject to the constraint of the deposit being connected. This interpretation antecipates the relation with random percolation, to be discussed in detail in Secs. IV and V.

IV. PORE SIZE DISTRIBUTION

Fig. 6 shows the pore size distributions of deposits grown with large R and with ϵ well below ϵ_c. For large pore sizes, they have exponential decays. This is what is typically expected in systems far from a critical point. Also note that the slopes of the fits in Fig. 6 decrease as ϵ increases, indicating that the average pore size increased.

Fig. 7 shows the pore size distribution of deposits grown with large R and two values of ϵ well above ϵ_c. A power law decay is observed:

$$P(s) \sim s^{-\Delta} \qquad , \qquad 1.35 \leq \Delta \leq 1.45. \tag{8}$$

Here, the error bar was obtained by fitting different ranges of the data for both values of ϵ shown in Fig. 7. This result contrasts to equilibrium phase transitions [31], in which power law decays are present only at the critical point (or may be observed in a narrow region around the critical point in finite-size samples).

In the critical point, the rapid adatom dynamics, of diffusive nature, tends to spread atoms upwards, i. e. to the empty region above the outer surface. This movement is only constrained by the connectivity condition, so that deposited atoms always form a cluster connected to the substrate. This suggests the structure of a critical percolation cluster.

Above the transition point, the adatom dynamics is even faster than that in the critical point. This favors random adatom distribution and stretches the cluster in the vertical direction under the connectivity constraint. Thus, we understand that the cluster is also set into a critical percolation structure by the dynamics. Due to the external adatom flux, this dynamics is certainly far from equilibrium. Consequently, its features may differ from those of equilibrium critical phenomena. However, as we explain below, the exponents are related to (statistical equilibrium) percolation exponents.

The critical percolation cluster can be divided in two parts: dead ends, which are isolated branches, and the backbone, which is the part that carries stress or current if the borders are mechanically or electrically excited [32]. Most of the mass of the cluster is in the dead ends. For this reason, while the fractal dimension of the cluster is $d_F = 91/48 \approx 1.89$ in two dimensions, the fractal dimension of the backbone is estimated as $d_B = 1.6432 \pm 0.0008$ [33].

The percolation backbone is frequently modelled as a system of links and blobs [34, 35]. The number of blobs of size b in a box with fixed lateral size is

$$n(b) \sim b^{-\tilde{\tau}}, \tag{9}$$

with

$$\tilde{\tau} = 1 + d_r/d_B, \tag{10}$$

where $d_r = 1/\nu$ is the exponent relating the number of blobs and the system size L, and $\nu = 4/3$ is the correlation length exponent of the problem [34, 36]. This gives $\tilde{\tau} \approx 1.45$.

The internal pores of the deposit are the pores surrounded by the blobs of this connected cluster. The blob size b is the number of particles (adatoms in our model) in the blob perimeter. The pore size s of our model is the area (number of empty sites) enclosed by the blob. Self-similarity implies that the large blobs have the same shape of the full backbone. If the blob occupies a region of linear size r, then the area and the perimeter are related as

$$s \sim b \sim r^{d_B}. \tag{11}$$

For this reason, one expects the same decay in the distributions (8) and (9), which gives

$$\Delta = \tilde{\tau}. \tag{12}$$

For comparison, Fig. 7 illustrates a decay with slope $\tilde{\tau}$. Our estimates of Δ are slightly smaller than this value. Possibly, this is related to the compact regions inside the largest pores, which gives an effective dimension of the area s [Eq. (11)] closer to 2 (consequently larger than d_B). It can be easily shown that the increase in this effective dimension leads to effective exponent Δ smaller than the predicted value.

In Sec. V B, we will show that the roughness scaling gives additional support to the interpretation that the structure of the deposits above the critical point is dominated by a percolation backbone.

V. SURFACE ROUGHNESS SCALING

A. Basics of kinetic roughening and universality classes

In systems with normal roughening (in opposition to anomalous roughening [37]), the expected scaling of the local roughness in large substrates is

$$w\left(r,t\right) \approx r^{\alpha} g\left(\frac{r}{t^{1/z}}\right), \tag{13}$$

where α and z are the roughness and dynamic exponents, respectively, and g is a scaling function. For $x \equiv r/t^{1/z} \ll 1$ (small box sizes), $g(x)$ is constant and $w \sim r^{\alpha}$; for $x \gg 1$ (large box sizes), the local roughness converges to the global one, $W\left(t\right)$, which scales as

$$W\left(t\right) \sim t^{\beta}, \tag{14}$$

with $\beta = \alpha/z$ called growth exponent (see Ref. [38] for a discussion of roughness scaling in several growth models).

Roughening dominated by adatom surface diffusion is generally believed to be described by fourth order stochastic growth equations in the continuous limit [8, 39]:

$$\frac{\partial h}{\partial t} = \nu_4 \nabla^4 h + \lambda_4 \nabla^2 (\nabla h)^2 + \eta(\vec{x},t), \tag{15}$$

where $h(\vec{x},t)$ is the height at position $\vec{x}$ and time t in a d-dimensional substrate, ν_4 and λ_4 are constants and η is a Gaussian (nonconservative) noise [a constant external particle flux is ommited from Eq. (15)]. For $\lambda_4 = 0$, Eq. (15) is linear and is usually called Mullins-Herring (MH) equation [40]. The nonlinear form ($\lambda_4 \neq 0$) is known as Villain-Lai-Das Sarma (VLDS) [41, 42] equation. In $d = 1$, the best estimates of VLDS exponents are obtained from conserved restricted solid-on-solid models: $\alpha = 0.94 \pm 0.02$, $z = 2.88 \pm 0.04$, and $\beta = 0.326 \pm 0.011$ [43].

In $d = 1$ and $d = 2$, renormalization studies [44] showed that the CV model belongs to the VLDS class. However, simulations show significant scaling corrections in $d = 1$ [45–48] and $d = 2$ [49].

On the other hand, most growth models that produce porous deposits are extensions of BD and are represented by the Kardar-Parisi-Zhang (KPZ) equation [50] in the hydrodynamic limit:

$$\frac{\partial h}{\partial t} = \nu_2 \nabla^2 h + \lambda_2 (\nabla h)^2 + \eta(\vec{x},t), \tag{16}$$

with ν_2 and λ_2 constant. In $d = 1$, KPZ exponents are $\alpha = 1/2$, $z = 3/2$, and $\beta = 1/3$.

The case $\lambda_2 = 0$ in Eq. (16) is the Edwards-Wilkinson [51] equation, with $\alpha = 0.5$ and $\beta = 0.25$ in $d = 1$. Refs. [18, 19] proposed that their activated surface diffusion models were in the EW universality class.

B. Simulation results

Fig. 8 shows the outer surface profiles of deposits grown with four pairs of parameters (R, ϵ) after deposition of 400 layers.

For small ϵ (Figs. 8a and 8b; $\epsilon = 0.01$), the interfaces show mounds separated by narrow deep valleys. These features are more prominent for large R (Fig. 8b), in which the mounds have small roughness and large widths. This is related to the large diffusion lengths of isolated adatoms in terraces. In this situation, the porosity is very small.

These trends are similar to the CV model and related collective diffusion models with solid-on-solid structure. Some interfaces generated by those models are shown in Refs. [45–47]: for low temperatures (small R and very small ϵ), the interfaces are rough, with rounded peaks separated by sharp deep valleys; as the temperature increases (large R and ϵ not very small), the width of the peaks increase and the roughness decreases; for high temperatures, the outer surface is very smooth.

Different features are observed above the transition temperature. Figs. 8c and 8d, for $\epsilon = 0.1$, show interfaces rough at short and large lengthscales, with narrow mounds for small and large R.

In Fig. 9a, we show the time evolution of the global roughness for deposits grown with two values of R below the transition point ($\epsilon = 0.01$). The interface smoothens as R increases, similarly to the CV model. For $R = 10$, the slope of the fit in Fig. 9a is near the VLDS exponent β. For $R = 10^3$, the slope of the fit is near the exponent β of the MH class [8, 40]. The MH exponents are also observed in some simulations of the CV model for large R [45–47] and are interpreted as an effect of a long crossover to VLDS scaling [44].

In Fig. 9b, we show the time evolution of the global roughness for deposits grown above the transition point ($\epsilon = 0.1$). In this case, increasing R slightly increases the roughness, in contrast to the trend of solid-on-solid models. The slopes of the linear fits are closer to the EW exponent $\beta = 0.25$. However, long range correlations are present in that case due to the no-desorption condition. Thus, the description of the interface evolution by local growth equations is expected to fail.

In Fig. 10, the local roughness $w\,(r, t = 400)$ is plotted as a function of the box size r for deposits grown above and below the transition point with $R = 10^3$.

The dominant slopes of those plots are calculated by a method proposed in Ref. [38]. First, the effective exponent $\alpha(r, t)$ is defined as the local slope of the $\log w\,(r, t) \times \log r$ plot. Then, the dominant slope is defined as the exponent α that minimizes $\left|\frac{d\alpha(r,t)}{d\log r}\right|$. The inset of Fig. 10 shows $|d\alpha/d\log r|$ as a function of α calculated using this procedure, showing minima at $\alpha \approx 0.75$ for $\epsilon = 0.01$ and $\alpha \approx 0.35$ for $\epsilon = 0.1$. In the main plot of Fig. 10, dashed lines have these slopes.

The initial slope ≈ 0.75 is dominant for $\epsilon = 0.01$. This is interpreted as an effect of the grainy interface structure shown in Figs. 8a,b, with wide and rough plateaus separated by narrow and deep valleys. For square surface blocks, the expected initial slope is 1 [52]. For rounded surface blocks, that slope is slightly smaller, typically between 0.7 and 1, which is the present case [53]. This is a geometric effect, with no relation to kinetic roughening.

The roughness saturates immediately after that initial regime, thus we cannot obtain a reliable estimate of the roughness exponent for $\epsilon = 0.01$. The VLDS roughness exponent is also large ($\alpha \approx 0.94$ [43]), thus a possible crossover may be hidden by the large initial slope. A long time crossover to KPZ scaling is also plausible because a small KPZ nonlinearity may be generated by the formation of overhangs and pores [9–16]. Also recall that slow crossovers to KPZ scaling are observed in the films with grainy interfaces of Refs. [52, 53], which resemble those in Figs. 8a,c,d.

For $\epsilon = 0.1$, a scaling region appears in Fig. 10 with slope ≈ 0.35, which differs from the roughness exponents α of EW, KPZ, MH, and VLDS classes. This is expected due to the long-range correlation introduced by the no-desorption conditions. On the other hand, the fractal dimension corresponding to this roughness (Hurst) exponent is $d_f = 2 - \alpha = 1.65$, which is in very good agreement with the dimension of the percolation backbone in two dimensions, $d_B \approx 1.6432 \pm 0.0008$ [33].

This result shows that the upper parts of the deposits above the transition point are also dominated by the structure (link-node-blob) of a percolation backbone. The contribution of the dead ends of the full percolation cluster is consequently negligible, which is reasonable for the scaling of the roughness at long wavelengths (large box size r). As explained in Ref. [8], the above self-similarity interpretation is also restricted to $r \ll L$, which is the case of the range of r fitting the slope 0.35 in Fig. 10.

We tried to improve the analysis of surface roughness scaling with alternative approaches, but

did not succeed. First, we used a method recently proposed to reduce the corrections to scaling in ballistic-like deposition models [54], but found no significant change in exponents β and α. Secondly, we measured roughness distributions in the growth regime. However, they had many fluctuations due to the small number of configurations calculated in a lattice size not very large, hindering a reliable comparison with distributions of KPZ, VLDS, and other growth classes.

VI. CONCLUSION

We studied a film growth model in two dimensions with temperature activated diffusion of adsorbed particles. The diffusion coefficient has the same form of the Clarke-Vvedensky model, but formation of overhangs and pores is allowed after an adatom step, with a no-desorption condition that rejects steps that lead to disconnection of one or more adatoms from the main deposit. The model was studied in $1+1$ dimensions due to computational limitations.

Taking the diffusion-to-deposition ratio R and the NN binding parameter ϵ as independent quantities, we show that a critical value ϵ_c separates regimes of low and high porosity. As R increases, the transition between these regimes becomes steeper as ϵ_c is crossed, with vanishingly small porosity for $\epsilon < \epsilon_c$ and finite porosity for $\epsilon > \epsilon_c$.

Taking fixed values of activation energies E_s and E_b, two regimes are separated by a transition temperature T_c, with porosity decreasing (increasing) with temperature for $T < T_c$ ($T > T_c$). If $E_s \sim E_b$, the value of R_c is very large and the transition temperature is of the order of E_b/k_B; this resembles the roughening transition in equilibrium models [8, 29].

The deposits grown with large R and $\epsilon > \epsilon_c$ are tuned into a critical percolation regime. The pore size distribution has a power-law decay, whose exponent is related to critical percolation exponents.

We also studied the kinetic roughening of the outer interface of the deposits. Below the transition point, growth exponents near the VLDS values are obtained, but a crossover to long time KPZ scaling cannot be discarded due to the small excess velocity provided by the formation of some small pores. Above the transition point, we obtain a roughness exponent $\alpha \approx 0.35$, which is related to the fractal structure of the percolation backbone.

Most of the results presented here are also expected if three-dimensional deposits are grown with this model. First, the transition in porosity is related only to the change in the mobility of adatoms with two or more neighbors. Second, the structure of the deposits at and above the transition point is also expected to be of a percolation backbone because this feature is related to the connectivity constraint and to the large adatom mobility. Third, the kinetic roughening of the outer surface will follow the same trend: below the transition point, VLDS scaling is also expected for the CV model in $2+1$ dimensions [44, 49], with a possible crossover to KPZ due to pore formation; above the critical point, the roughness exponent is also expected to be related to the percolation cluster structure. On the other hand, the pore size distribution may change drastically in $2+1$ dimensions because the density of the deposits will be much smaller and the pore space will probably be infinitely connected (this is the case, for instance, of ballistic deposits [13–15]).

Our results suggest that adsorbed molecule diffusion may also be considered to explain increase of porosity in thin films, in contrast to the usual expectation that more compact and smoother films are obtained as the temperature increases. This unusual trend was already observed in electrostatic spray deposition of oxides [21, 22], but other mechanisms were considered to explain those features, such as the evaporation of the spray droplets.

ACKNOWLEDGMENTS

This work was partially supported by CNPq and FAPERJ (Brazilian agencies).

[1] T. J. Barton, L. M. Bull, W. G. Klemperer, D. A. Loy, B. McEnaney, M. Misono, P. A. Monson, Guido Pez, G. W. Scherer, J. C. Vartuli, and O. M. Yaghi, Chem. Mater. **11**, 2633 (1999).
[2] R. Hilfer, in Advances in Chemical Physics, Vol. XCII, eds. I. Prigogine and S. A. Rice (Wiley, Chichester, UK, 1996).
[3] W. Xuan, C. Zhu, Y. Liu, and Y. Cui, Chem. Soc. Rev. **41**, 1677 (2012).
[4] P. Innocenzi, L. Malfatti, and G. J. A. A. Soler-Illia, Chem. Mater. **23**, 2501 (2011).
[5] J. Huang, G. Orkoulas, and P. D. Christofides, Chem. Eng. Sci. **74**, 135 (2012).
[6] J. Huang, G. Orkoulas, and P. D. Christofides, Chem. Eng. Sci. **94**, 44 (2013).
[7] M. J. Vold, J. Coll. Sci. **14**, 168 (1959); J. Phys. Chem. **63**, 1608 (1959).
[8] A. L. Barabási and H. E. Stanley, *Fractal concepts in surface growth* (Cambridge University Press, Cambribge, England, 1995).
[9] Y. P. Pellegrini and R. Jullien, Phys. Rev. Lett. **64** 1745 (1990).
[10] M. E. Kainourgiakis, T. A. Steriotis, E. S. Kikkinides, G. Romanos, and A. K. Stubos, Colloids and Surfaces A **206**, 321 (2002).
[11] S. Tarafdar and S. Roy, Physica B **254**, 28 (1998).
[12] D. Rodríguez-Pérez, J. L. Castillo, and J. C. Antoranz, Phys. Rev. E **72** 021403 (2005).
[13] J. Yu and J. G. Amar, Phys. Rev. E **65**, 060601(R) (2002).
[14] F. A. Silveira and F. D. A. Aarão Reis, Phys. Rev. E **75**, 061608 (2007).
[15] K. Khanin, S. Nechaev, G. Oshanin, A. Sobolevski, and O. Vasilyev, Phys. Rev. E **82**, 061107(R) (2010).
[16] K. Banerjee, J. Shamanna, and S. Ray, Phys. Rev. E **90**, 022111 (2014).
[17] J. W. Evans, P. A. Thiel, and M. C. Bartelt, Surf. Sci. Rep. **61**, 1 (2006).
[18] G. Hu, J. Huang, G. Orkoulas, and P. D. Christofides, Phys. Rev. E **80**, 041122 (2009).
[19] X. Zhang, G. Hu, G. Orkoulas, and P. D. Christofides, Chem. Eng. Sci. **65**, 4720 (2010).
[20] M. Ohring, *Materials Science of Thin Films - Deposition and Structure*, 2nd. ed., Academic Press, 2001.
[21] C. Chen, E. M. Kelder, P. J. J. M. van der Put, and J. Schoonman, J. Mater. Chem. **6**, 765 (1996).
[22] D. Marinha, L. Dessemond, J. S. Cronin, J. R. Wilson, S. A. Barnett, and E. Djurado, Chem. Mater. **23**, 5340 (2011).
[23] S. Clarke and D. D. Vvedensky, J. Appl. Phys. **63**, 2272 (1988).
[24] C. Ratsch, A. Zangwill, P. Smilauer, and D. D. Vvedensky, Phys. Rev. Lett. **72**, 3194 (1994).
[25] Y. Shim and J. G. Amar, Phys. Rev. B **71**, 125432 (2005); J. Chem. Phys. **134**, 054127 (2011).
[26] T. J. Oliveira and F. D. A. Aarão Reis, Phys. Rev. B **87**, 235430 (2013).
[27] J. Hoshen and R. Kopelman, Phys. Rev. B. **14**, 3438 (1976).
[28] A. Giri, S. Tarafdar, P. Gouze, and T. Dutta, Geophys. J. Int. **192**, 1059 (2013).
[29] J. D. Weeks and G. H. Gilmer, Adv. Chem. Phys. **40**, 157 (1979).
[30] P. A. Sánchez, T. Sintes, J. H. E. Cartwright, and O. Piro, Phys. Rev. E **81**, 011140 (2010).
[31] J. J. Binney, N. J. Dowrick, A. J. Fisher, and M. E. J. Newman, *The Theory of Critical Phenomena. An Introduction to the Renormalization Group* (Oxford University Press, Oxford, 1992).
[32] D. Stauffer and A. Aharony, *Introduction to Percolation Theory*, 2nd. edition (Taylor & Francis, London/Philadelphia, 1992).
[33] P. Grassberger, Physica A **262**, 251 (1999).
[34] H. J. Herrmann and H. E. Stanley, Phys. Rev. Lett. **53**, 1121 (1984).
[35] M. Barthelemy, S. V. Buldyrev, S. Havlin, and H. E. Stanley, Phys. Rev. E **60**, R1123 (1999).
[36] A. Coniglio, Phys. Rev. Lett. **46**, 250 (1981); J. Phys. A: Math. Gen. **15**, 3829 (1982).
[37] J. J. Ramasco, J. M. López, and M. A. Rodríguez, Phys. Rev. Lett. **84**, 2199 (2000).
[38] A. Chame and F. D. A. Aarão Reis, Surf. Sci. **553**, 145 (2004).
[39] J. Krug, Adv. Phys. **46**, 139 (1997).
[40] W. W. Mullins, J. Appl. Phys. **28**, 333 (1957); C. Herring, in *The Physics of Powder Metallurgy*, ed. W. E. Kingston (McGraw-Hill, New York, 1951).

[41] J. Villain, J. Phys. I **1**, 19 (1991).
[42] Z.-W. Lai and S. Das Sarma, Phys. Rev. Lett. **66**, 2348 (1991).
[43] F. D. A. Aarão Reis, Phys. Rev. E **70**, 031607 (2004).
[44] C. A. Haselwandter and D. D. Vvedensky, Europhys. Lett. **77**, 38004 (2007); Phys. Rev. E **77**, 061129 (2008).
[45] P. I. Tamborenea and S. Das Sarma, Phys. Rev. E **48**, 2575 (1993).
[46] S. Das Sarma, C. J. Lanczycki, R. Kotlyar, and S. V. Ghaisas, Phys. Rev. E **53**, 359 (1996).
[47] M. Kotrla and P. Smilauer, Phys. Rev. B **53**, 13777 (1996).
[48] B. Meng and W. H. Weinberg, Surf. Sci. **364**, 151 (1996).
[49] M. R. Wilby, D. D. Vvedensky, and A. Zangwill, Phys. Rev. B **46**, 12896(R) (1992).
[50] M. Kardar, G. Parisi and Y.-C. Zhang, Phys. Rev. Lett. **56**, 889 (1986).
[51] S.F. Edwards and D.R. Wilkinson, Proc. R. Soc. London **381**, 17 (1982).
[52] T. J. Oliveira and F. D. A. Aarão Reis, J. Appl. Phys. **101**, 063507 (2007).
[53] T. J. Oliveira and F. D. A. Aarão Reis, Phys. Rev. E **83**, 041608 (2011).
[54] S. G. Alves, T. J. Oliveira, and S. C. Ferreira, Phys. Rev. E **90**, 052405 (2014).

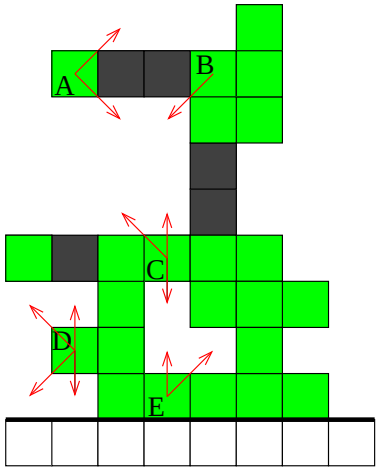

FIG. 1. (Color online) Schematic representation of the growing layer: substrate sites are empty squares, mobile adatoms are colored (green) squares, and non-mobile adatoms are black squares. The allowed steps of five adatoms, labeled A to E, are indicated by red arrows.

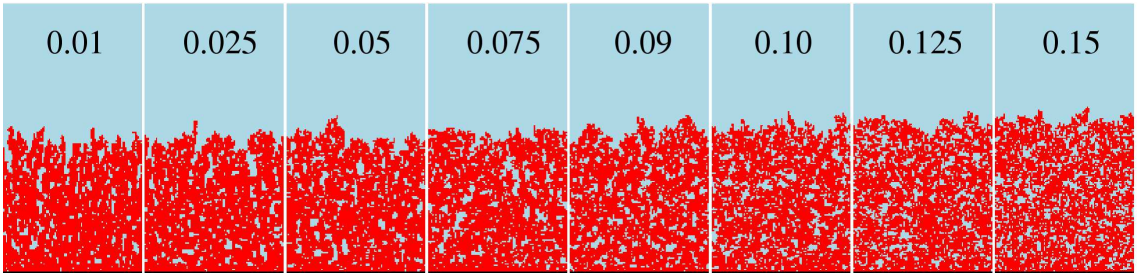

FIG. 2. (Color online) Snapshots of the layer in 100-site wide regions, for $R = 10$ and values of ϵ indicated on the figure.

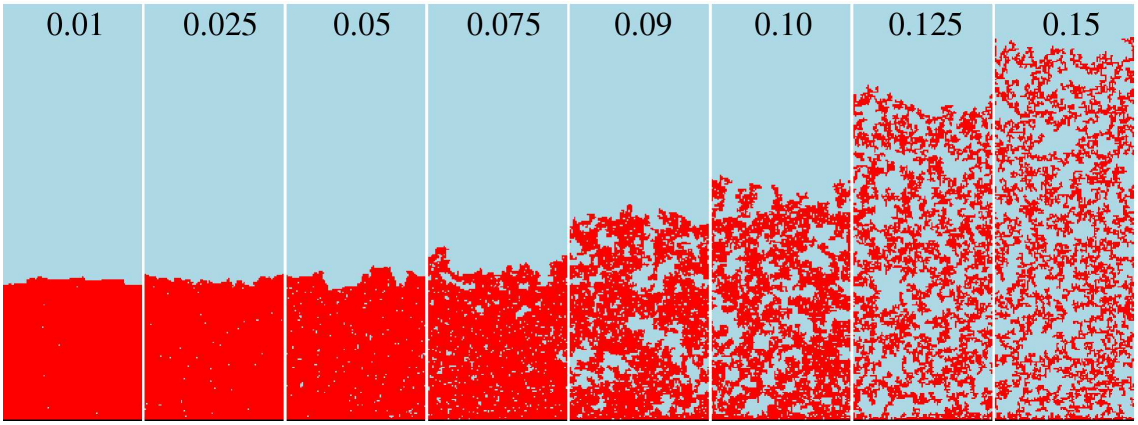

FIG. 3. (Color online) Snapshots of the layer in 100-site wide regions, for $R = 10^4$ and values of ϵ indicated on the figure.

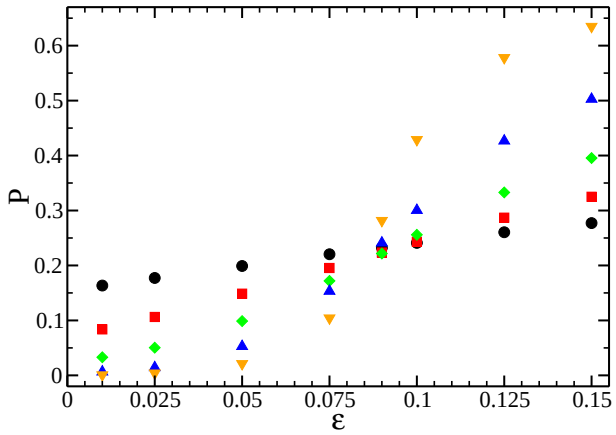

FIG. 4. (Color online) Porosity as a function of ϵ for $R = 10$ (black circles), $R = 50$ (red squares), $R = 200$ (green diamonds), $R = 10^3$ (blue up triangles), and $R = 10^4$ (yellow down triangles).

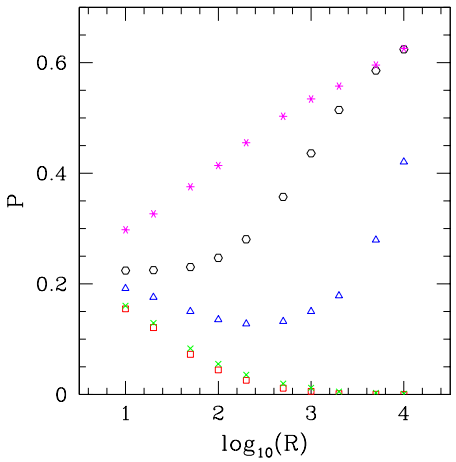

FIG. 5. (Color online) Porosity as a function of R for several ratios E_s/E_b: 1 (red squares), 5 (green crosses), 8 (blue triangles), 10 (black hexagons), and 15 (magenta asterisks).

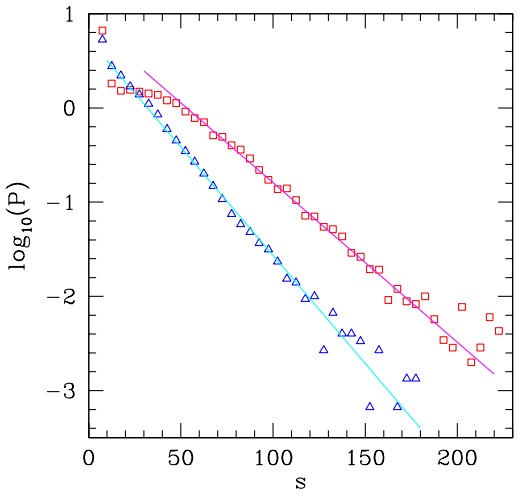

FIG. 6. (Color online) Pore size distribution below the transition point, for $R = 10^3$ and $\epsilon = 0.01$ (triangles) and $\epsilon = 0.025$ (squares) (data not normalized). Solid lines are least squares fits of the data in the approximately linear regions.

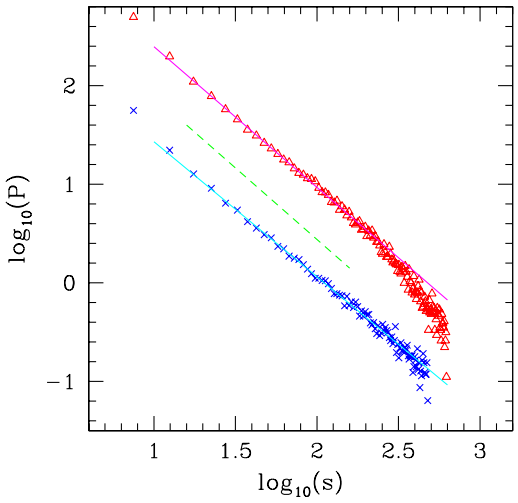

FIG. 7. (Color online) Pore size distribution (not normalized) above the transition point, for $\left(R = 10^3, \epsilon = 0.125\right)$ (red triangles) and $\left(R = 10^3 \epsilon = 0.15\right)$ (blue crosses). The linear fits (solid lines) have slopes -1.43 and -1.37, respectively. The dashed line has slope -1.45.

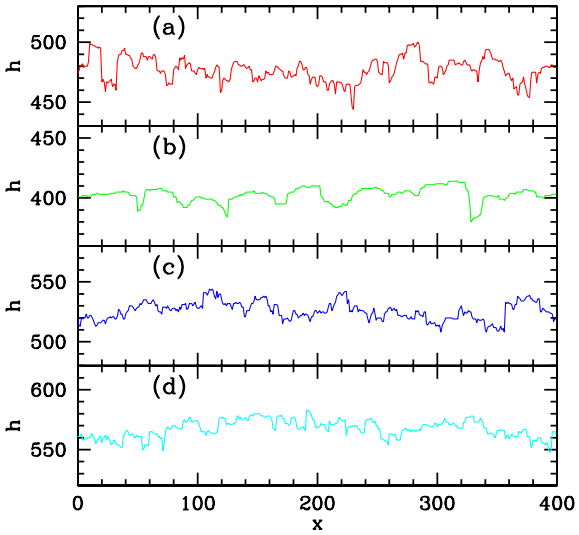

FIG. 8. (Color online) Outer interface profiles after deposition of 400 layers with (a) $R = 10$, $\epsilon = 0.01$, (b) $R = 10^3$, $\epsilon = 0.01$, (c) $R = 10$, $\epsilon = 0.1$, (d) $R = 10^3$, $\epsilon = 0.1$.

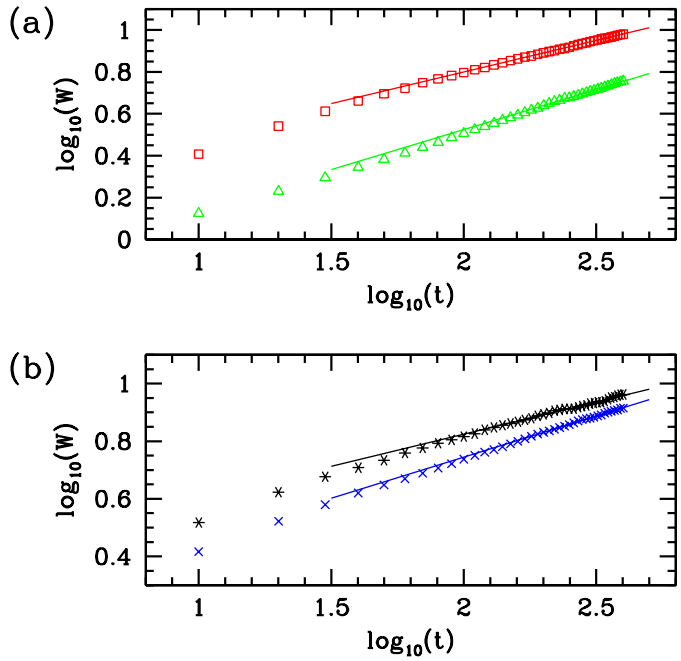

FIG. 9. (Color online) Global roughness as a function of time and corresponding least squares fits (solid lines) for: (a) $\epsilon = 0.01$, $R = 10$ (red squares; slope 0.30) and $R = 10^3$ (green triangles; slope 0.38); (b) $\epsilon = 0.1$, $R = 10$ (blue crosses; slope 0.29) and $R = 10^3$ (black asterisks; slope 0.22).

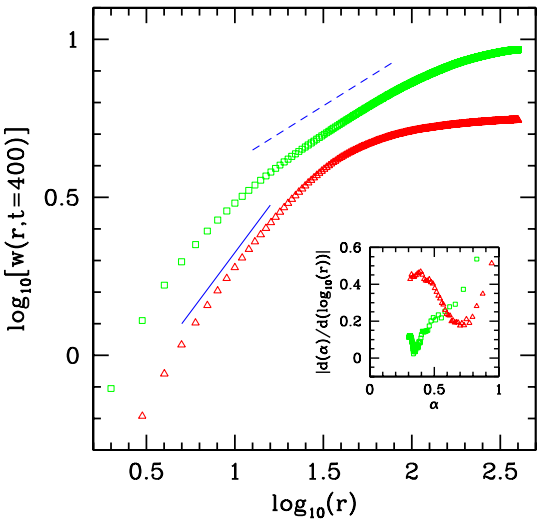

FIG. 10. (Color online) Local roughness of deposits grown with $R = 10^3$ and $\epsilon = 0.01$ (red triangles) and $\epsilon = 0.1$ (green squares). Solid and dashed lines are drawn to guide the eye and have slopes 0.75 and 0.35, respectively. Inset: $|d\alpha/d\log r|$ as a function of α, with symbols corresponding to the same parameters of the main plot.